Chemical Engineering Journal 437 (2022) 135394

Contents lists available at ScienceDirect

Chemical Engineering Journal

journal homepage: www.elsevier.com/locate/cej

Integrated carbon capture and utilization: Synergistic catalysis between highly dispersed Ni clusters and ceria oxygen vacancies

Hongman Sun [a,b], Yu Zhang [a], Chunfen Wang [a], Mark A. Isaacs [c,d], Ahmed I. Osman [b], Yehong Wang [e], David Rooney [b], Youhe Wang [a], Zifeng Yan [a], Christopher M.A. Parlett [f,g,h,i,*], Feng Wang [e,*], Chunfei Wu [b,*]

[a] College of Chemistry and Chemical Engineering, State Key Laboratory of Heavy Oil Processing, China University of Petroleum, Qingdao 266580, PR China
[b] School of Chemistry and Chemical Engineering, Queen's University Belfast, Belfast BT7 1NN, UK
[c] Department of Chemistry, University College London, London WC1H 0AJ, UK
[d] Harwell XPS, Research Complex at Harwell, Rutherford Appleton Laboratory, Didcot OX11 0FA, UK
[e] State Key Laboratory of Catalysis, Dalian National Laboratory for Clean Energy, Dalian Institute of Chemical Physics, Chinese Academy of Sciences, Dalian 116023, PR China
[f] Department of Chemical Engineering and Analytical Science, University of Manchester, Manchester M13 9PL, UK
[g] Diamond Light Source, Harwell Science and Innovation Campus, Didcot OX11 0DE, UK
[h] The University of Manchester at Harwell, Diamond Light Source, Harwell Science and Innovation Campus, Didcot OX11 0DE, UK
[i] UK Catalysis Hub, Research Complex at Harwell, Rutherford Appleton Laboratory, Harwell OX11 0FA, UK

ARTICLE INFO

Keywords:
Sub-nanometer catalysts
Oxygen vacancies
Carbon capture
Methane
CeO_2

ABSTRACT

Integrated carbon capture and utilization (ICCU) presents an ideal solution to address anthropogenic carbon dioxide (CO_2) emissions from industry and energy sectors, facilitating CO_2 capture and subsequent utilization through conversion into high-value chemicals, as opposed to current release into the atmosphere. Herein, we report the synergistic coupling of porous CaO, as a sorbent for CO_2 capture, and Ni doped CeO_2 nanorods, as catalytic sites for CO_2 reduction. It is found that ceria is shown to possess the capacity for CO_2 utilization, however, critically it only results in the generation of CO due to the weak CO-ceria bonding. The addition of Ni active sites gives rise to CH_4 being the predominant product, via the strong interaction between Ni species and CO, which facilitates further reduction. Through tuning Ni loadings, we have evaluated the role of catalytic active site size, with a Ni loading of only 0.5 wt% providing optimal performance through the formation of sub-nanometer sized clusters. This near-atomic active site dispersion gives rise to CH_4 productivity and selectivity of 1540 mmol g^{-1} Ni and 85.8%, respectively, with this optimal combination of catalyst and sorbent demonstrating high stability over 10 cycles of ICCU process. These observations in parallel with the synergistic coupling of earth-abundant, low-cost materials (CaO and Ni) will have broad implications on the design and implementation of high efficiency, cost-effective ICCU materials and processes.

1. Introduction

Atmospheric carbon dioxide (CO_2) concentrations have undergone extraordinary increases from 310 to 416 ppm in the past half-century primarily because of fossil fuel combustion [1–3]. Carbon capture and utilization (CCU) has drawn intensive interest due to its capacity to sequester CO_2 and utilise it as a source of carbon to produce high-value chemicals and fuels, and thus promote a circular economy while mitigating against climate change [4,5]. However, state-of-the-art CCU exhibits poor economics and technological complexity due to extensive energy input, a multiple reactor configuration, and sorbent transfer between reactors, to allow temperature or pressure swing sorbent regeneration [6,7]. Recently, promising integrated carbon capture and utilization (ICCU) has emerged as a lower-cost alternative technology, with captured CO_2 converted into value-added products, e.g. CO and CH_4, within a single reactor under isothermal conditions [8,9]. During ICCU, two steps are involved: 1st step is carbon capture from flue gas using an adsorbent, subsequently the captured CO_2 is rapidly converted over catalytic sites in the 2nd step [10–14]. The integration of these steps offers potential improvements in efficiency and cost-effectiveness, while

* Corresponding authors.
E-mail addresses: christopher.parlett@manchester.ac.uk (C.M.A. Parlett), wangfeng@dicp.ac.cn (F. Wang), c.wu@qub.ac.uk (C. Wu).

https://doi.org/10.1016/j.cej.2022.135394
Received 2 December 2021; Received in revised form 14 February 2022; Accepted 18 February 2022
Available online 23 February 2022

allowing a one reactor process under isothermal conditions. Thus, the development of materials and systems that can capture CO_2 and facilitate its conversion to other high-value chemicals at the same temperature is highly desirable [15,16].

CaO is regarded as a promising carbon capture material due to its high theoretical CO_2 uptake of 17.8 mmol g^{-1} and low cost [17–19]. Duyar et al. employed nano-dispersed CaO on alumina, produced via simple wet impregnation, as the sorbent [9], whilst Arellano-Treviño et al. investigated alkaline and alkaline earth oxides as sorbents, identifying CaO to be a reasonable sorbent candidate [13]. Noble metals, specifically Ru [9,13] and Rh [20], supported over high surface area oxide such as Al_2O_3 are commonly deployed as catalysts because of their high activity and selectivity in CO_2 conversion to CH_4. Ru based systems have been reported by Duyar and co-workers, and Bermejo-López et al. [9,12], both coupled with CaO sorbent in dual functional materials, in which catalysts and sorbent were deposited on a single support, for isotherm capture and conversion. While Bermejo reported an optimal methane production of 414 μmol g^{-1} at 400 °C, Duyar show excellent stability at 320 °C over 11 capture and conversion cycles (average methane production 283 μmol g^{-1}). Unfortunately, the high cost of noble metals and potential poor resistance to pollutants are drawbacks that may hinder their widespread deployment [21]. Earth-abundant metals, such as nickel, are promising alternative catalytic sites for ICCU, due to cost-effectiveness, and critically that they enable a temperature window for catalysis which is compatible to that required for CO_2 capture [22,23]. However, Arellano-Treviño et al. observed that at lower ICCU process temperature (320 °C), Ni-based catalyst sites were not reduced to the active state, resulting in poor performance compared to Ru or Rh [13]. Thus, catalysts and process conditions require further development for efficient and cost-effective ICCU to be realised.

Active site miniaturisation provides a route to enhance catalytic performance through escalating active site density. Theoretical and experimental studies have revealed the prospect of sub-nanometer metallic active sites, offering superior catalytic activity and selectivity [24,25], while maximizing the efficiency of metal utilization, and fine-tuning active site environmental structure [26]. However, highly dispersed metal sites can display high mobility at elevated temperatures, leading to agglomeration due to their high surface energy [27]. Addressing the above challenges, downsizing metal catalytic sites to sub-nanometer scale while anchoring them on the supports is highly desirable and critical to efficient and cost-effective ICCU processes [28]. Among various metal oxides, e.g. Al_2O_3, SiO_2, and TiO_2, used as supports in methanation catalysis, CeO_2 has drawn intensive attention due to its basic nature, high stability, and capacity for oxygen vacancy formation [29,30]. These vacancies can directly dissociate CO_2 to CO*, and thus provide a pathway to initiate and enhance CO_2 conversion [8,31], while a high affinity between surface lattice oxygen and metal atoms can stabilize guest cations, maintaining high metal dispersion on CeO_2 support [32]. However, a detailed understanding of such interaction between highly dispersed metal clusters sites and CeO_2 support sites is lacking, as is insight into the reaction mechanism. This absence of knowledge retards the rational design of efficient materials utilized in the ICCU process, and therefore addressing these deficiencies in knowledge is paramount.

Herein we report the synthesis of effective materials for capture (CaO sorbents) and utilisation (sub-nanometer Ni doped CeO_2 nanorods), and their combination as a physical mixture used in the ICCU process for methane production. The process, depicted in Scheme 1, comprises a capture cycle, in which CO_2 from flue gas is adsorbed by CaO to produce $CaCO_3$, under the subsequent utilisation cycle, in which gas feed switch to a hydrogen-rich stream, the captured CO_2 was converted into methane over Ni/CeO_2 catalyst.

2. Experimental

2.1. Preparation of catalysts

A hydrothermal process, as previously reported, was used to synthesize CeO_2 nanorods [33]. Typically, 1.730 g cerium nitrate hexahydrate ($Ce(NO_3)_3{\cdot}6H_2O$) and 20.0 g of sodium hydroxide (NaOH) were dissolved in 10 mL and 70 mL of deionized water to get the solution A and B, respectively. The mixture obtained by adding solution A into solution B was stirred for 30 min at room temperature, and then transferred into a stainless-steel autoclave (100 mL) and maintained at 100 °C for 24 h. After cooling down to room temperature, the products were separated by centrifugation and then washed with water until the pH reached 7 and dried at 80 °C overnight to obtain CeO_2 nanorods.

A wet impregnation method was used to prepare CeO_2 supported catalysts. Typically, a predetermined amount of nickel nitrate hexahydrate $Ni(NO_3)_2{\cdot}6H_2O$, corresponding to 0.5 wt%, 1 wt% and 5 wt% of Ni was dissolved into 16 mL deionized water and then 0.8 g CeO_2 nanorods were added. The mixture solution was stirred at room temperature for 8 h, before the evaporation of water at 80 °C and then dried overnight. The samples were reduced at 550 °C in 5% H_2/N_2 for 3 h at a heating rate of 2 °C min^{-1}, and are identified as 0.5%Ni/CeO_2, 1%Ni/CeO_2 and 5%Ni/CeO_2, respectively. When the heating rate increased to 10 °C min^{-1}, the catalyst is designated 5%Ni/CeO_2-10. The reduction temperature was determined by H_2-TPR of the synthesized materials (isolated before reduction), as shown in Fig. S1, with nickel nitrate fully reduced below 550 °C. H_2-TPR was carried out on VDSorb-91i purchased from Quzhou

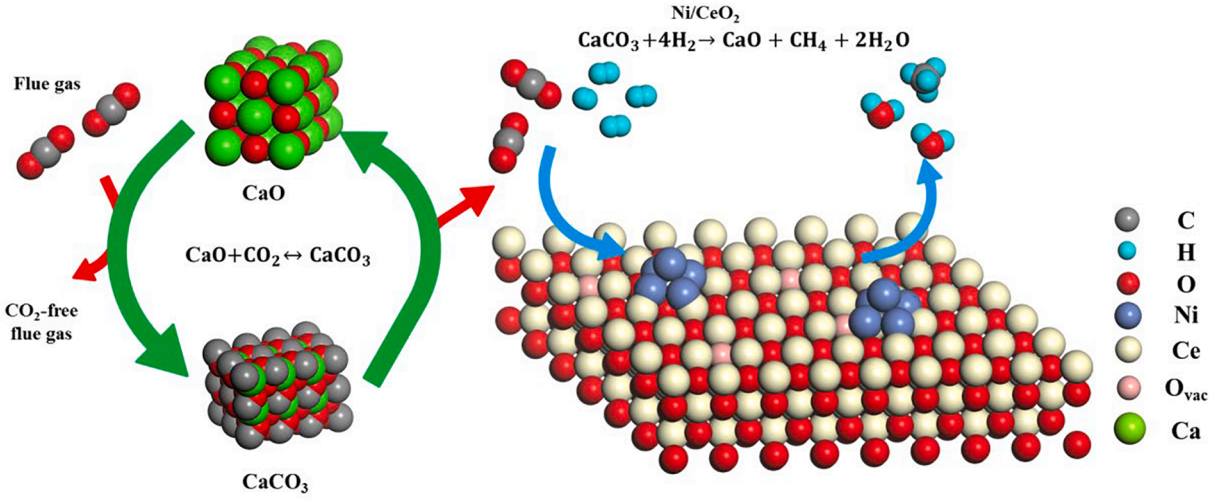

Scheme 1. Schematic illustrating the role of CaO sorbent and highly dispersed Ni clusters supported on CeO_2 nanorods during ICCU.

Vodo Instrument Co. Ltd. 100 mg of synthesized catalyst was placed into a U-shape tube and pre-treated at 100 °C for 30 min in pure N_2. After cooling to 50 °C, H_2-TPR was conducted under 5% H_2/N_2 (30 mL min^{-1}) at a heating rate of 10 °C min^{-1} up to 800 °C.

2.2. Preparation of adsorbent

A standard sol–gel process proposed by Santos et al. was used to synthesize a CaO adsorbent [34]. A predetermined amounts of calcium nitrate tetrahydrate ($Ca(NO_3)_2{\cdot}4H_2O$) and citric acid monohydrate ($C_6H_8O_7{\cdot}H_2O$) acting as chelation agent, were added to the deionized water at room temperature (water and citric acid to metal ion molar ratios were 40:1 and 1:1, respectively). The mixture was continuously stirred at 80 °C to form a translucent pale-yellow sol with good dispersion. After drying the prepared sol overnight at 130 °C, the translucent pale-yellow sol turned into low-density foam. The obtained foam was then calcined in a muffle furnace at 850 °C for 2 h at a heating rate of 2 °C min^{-1}. This synthesized sample was designated as sol–gel CaO. A detailed investigation into the CaO adsorbent, including extensive characterisation and the carbonation mechanism can be found in our previous publication [35].

2.3. Material characterizations

The Ni loadings were determined by an inductively coupled plasma optical emission spectrometry (ICP-OES, Agilent 720).

High-resolution transmission electron microscopy (HRTEM) and high-angle annular dark-field scanning transmission electron microscopy (HAADF-STEM) measurements coupled with EDX were performed on a TALOS F200X G2 microscope, operating at an acceleration voltage of 200 kV. Powder samples were prepared for imagining by dispersing in methanol and deposited to dry holey carbon grids.

Powder X-ray diffraction (XRD) patterns ranging from 10 to 80° were collected by a PANalytical empyrean series 2 diffractometer with Cu Ka X-ray source. XRD data were analysed by X'pert Highscore plus software.

X-ray absorption spectroscopy (XAS) at Ni K-edge (8.3 keV) were recorded at the B18 beamline of the Diamond Light Source, UK, using Si (1 1 1) double crystal monochromator. The catalysts were pelletised with boron nitride. All samples were collected in fluorescence mode, while standards were collected in transmission. Ni foil spectra were simultaneously collected to samples and standards to enable energy calibrations. Data processing was carried out using Demeter open source software package, version 0.9.26, with XAS spectra processing (normalization and background subtractions) and extended X-ray absorption fine structure (EXAFS) fitting conducted within the Athena and Artemis programs, respectively.

XPS data were acquired using a Kratos Axis SUPRA using monochromated Al kα (1486.69 eV) X-rays at 12 mA emission and 15 kV HT (180 W) and a spot size/analysis area of 700 × 300 μm. The instrument was calibrated to gold metal Au 4f (83.95 eV) and dispersion adjusted to give a BE of 932.6 eV for the Cu $2p_{3/2}$ line of metallic copper. Ag $3d_{5/2}$ line FWHM at 10 eV pass energy was 0.544 eV. Source resolution for monochromatic Al Kα X-rays is ~ 0.3 eV. The instrumental resolution was determined to be 0.29 eV at 10 eV pass energy using the Fermi edge of the valence band for metallic silver. Resolution with charge compensation system on < 1.33 eV FWHM on PTFE. High-resolution spectra were obtained using a pass energy of 20 eV, step size of 0.1 eV and sweep time of 60 s, resulting in a line width of 0.696 eV for Au $4f_{7/2}$. Survey spectra were obtained using a pass energy of 160 eV. Charge neutralisation was achieved using an electron flood gun with filament current = 0.38 A, charge balance = 2 V, filament bias = 4.2 V. Successful neutralisation was adjudged by analysing the C 1s region wherein a sharp peak with no lower BE structure was obtained. Spectra have been charge corrected to the mainline of the carbon 1 s spectrum (adventitious carbon) set to 284.8 eV. All data was recorded at a base pressure of below 9×10^{-9} Torr and a room temperature of 294 K. Data was analysed using CasaXPS v2.3.19PR1.0. Peaks were fit with a Shirley background before component analysis. Ni core-lines were fit using the Gupta and Sen multiplet approximation for free ion Ni^{2+} [36], while satellites were fit using an LA(1.53, 253) lineshape. Ceria $^{3+/4+}$ ratio was determined according to the fits derived by Romeo *et al.* [37].

Ni dispersion was calculated by CO chemisorption performed on Micromeritics Autochem II 2920 analyser. Typically, 100 mg of as-synthesised catalyst was reduced at 550 °C for 30 min at a heating rate of 10 °C min^{-1} in a U-shape quartz tube. The temperature was further increased to 600 °C under pure He for 60 min to remove the absorbed H_2. 1% CO/He and He were used for the loop gas and carrier gas, with pulse chemisorption measurement conducted at 35 °C.

Raman spectra were acquired by a Raman spectrometer purchased from WITec, Ulm, Germany equipped with a 532 nm diode laser with a total accumulation time of 20 s.

Both TGA (in N_2 atmosphere) and TPO (in air atmosphere) with the corresponding derivative weight are conducted by Thermo Gravimetric Analyzer (METTLER TOLEDO TGA/DSC 3 + LF/1100/704) for the characterization of carbonate level and coke deposition, respectively. Around 10 mg sample was heated from room temperature to 900 °C in air (flow rate, 50 mL min^{-1}) with a heating rate of 10 °C min^{-1}.

In-situ DRIFTs experiments were conducted by an FTIR spectrometer (vertex 70v, Bruker) coupled with a DRIFTs cell (homemade). All spectra were recorded over accumulative 32 scans with a resolution of 4 cm^{-1} in the range of 4000–400 cm^{-1}. The reduced sample (~5 mg) was increased to 550 °C in N_2 atmosphere. And then the carbonation was performed in CO_2 or CO for 30 min or 18 min, respectively. Subsequently, the feed gas was switched to 10% H_2 balanced with N_2 for the conversion after the in-situ reactor was purged by N_2 for 3 min.

In situ IR spectra were collected on a Bruker Tensor 27 instrument. The samples were pressed into a self-supporting disk with a diameter of 13 mm and placed into the IR cell. Firstly, the sample was reduced at 350 °C in H_2 for 30 min before being cooled to room temperature to collect a background spectrum. CO was then introduced into the IR cell for 30 min and sequentially purged by Ar at room temperature, with the IR spectrum of chemisorbed CO recorded at room temperature.

2.4. ICCU performance evaluation

ICCU was performed in a vertical fixed-bed reactor at atmospheric pressure, and the process diagram is described in Fig. S2. Typically, a predetermined amount of a physical mixture of CaO adsorbent (0.3 g) and Ni/CeO_2 catalyst (0.3 g), a mass ratio of 1:1, was mixed with 1.0 g of quartz sand was loaded into the reactor. Carbon capture was conducted in 15% CO_2/N_2 (50 mL min^{-1}), to mimic flue gas, at 550 °C for 60 min (1^{st} step). The reactor was then purged with pure N_2 for 5 min (50 mL min^{-1}). The feed gas was then switched to H_2 (50 mL min^{-1}) to convert the captured CO_2 into CH_4 for 60 min (2^{nd} step). The process was under isothermal conditions throughout. Unreacted substrate and products of the carbon capture and conversion stages were collected in gas bags separately and analysed by off-line gas chromatography (GC, Techcomp 7900, TCD detector, TDX-01 column) with N_2 as an internal standard. The CO_2 capture capacity is defined as the difference between the recorded CO_2 concentrations in the outlet gas stream in the presence of a sorbent and a blank experiment without a CO_2 sorbent. The calculation of carbon balance, CO_2 conversion, CH_4 selectivity, is described as follows:

$$\text{Carbon balance} = \frac{CH_4 \text{ yield} + CO_2 \text{ yield} + CO \text{ yield}}{CO_2 \text{ capture capacity}} \quad (1)$$

$$CO_2 \text{ conversion} = \frac{CH_4 \text{ yield} + CO \text{ yield}}{CO_2 \text{ capture capacity}} \quad (2)$$

$$CH_4\ \text{selectivity} = \frac{CH_4\ \text{yield}}{CH_4\ \text{yield} + CO\ \text{yield}} \quad (3)$$

2.5. DFT calculations

DFT calculations were carried out with a periodic plane wave using the Vienna ab initio simulation package (VASP) [38]. The exchange–correlation potentials were described within the generalized gradient approximation (GGA) in the form of Perdew-Burke-Ernzerhof (PBE) [39]. The projector augmented wave (PAW) method was utilized to describe the electron–ion interactions [40]. During the structure relaxation, the convergence criterion was set to 0.03 eV/Å and 10^{-5} eV for the residual force and energy, respectively. A 2 × 3 supercell of CeO_2(1 1 0) with an oxygen vacancy was used as the CeO_2 substrate. The Brillouin zones were sampled by a 3 × 3 × 1 Monkhorst-Pack k-point mesh. To avoid the interaction between two periodic units, a vacuum space of 15 Å was employed.

The adsorption energy of CO was calculated by:

$$E_b = E_{*CO} - E_* - E_{CO} \quad (4)$$

Where E_{*CO} and E_* are the energies of systems with and without the adsorption of CO, and the E_{CO} is the energy of a CO molecule in the gas phase. Therefore, a more negative E_b indicates a stronger adsorption strength of CO.

3. Results and discussion

3.1. Characterization of sorbent and catalysts

The structure of CaO sorbent and pristine CeO_2 were examined by TEM, as presented in Fig. S3. The porous structure of CaO sorbents is confirmed in Fig. S3a, which is in agreement with the literature and results from the addition of citric acid to the sol–gel method [34]. This material has previously demonstrated excellent performance for carbon capture [41,42]. The CeO_2 support presents as nanorods with a width and length spanning 10 to 20 nm and 100 to 200 nm, respectively, as shown in Fig. S3b, which concurs with the originally reported synthesis [33]. The support morphology and highly crystalline nature are unaffected by Ni doping as shown in Fig. 1, with an interplanar spacing of 0.19 nm attributed to the CeO_2 (1 1 0) phase, present for all Ni loadings. ICP-OES results (Table 2) show Ni loadings are 0.3 wt%, 0.6 wt%, 3.8 wt % and 3.7 wt% in 0.5%Ni/CeO_2, 1%Ni/CeO_2, 5%Ni/CeO_2 and 5%Ni/CeO_2-10, respectively. The numbers are slightly lower than the theoretical values. This is because the samples were prepared by the impregnation method and ICP is used to determine the Ni content of the bulk phase. STEM-EDX elemental mapping was applied to determine the distribution of Ni within the synthesized catalysts. A uniform Ni elemental distribution in both 0.5%Ni/CeO_2 (Fig. 1c) and 1%Ni/CeO_2 (Fig. 1f) confirms that NiO is well dispersed on the CeO_2 nanorod supports. Further increasing Ni loading to 5 wt%, the interplanar spacing of 0.21 nm is observed in Fig. 1g, which is corresponding to NiO (200) lattice plane. In addition, a more concentrated Ni elemental distribution is shown in 5%Ni/CeO_2 (Fig. 1i) indicating the formation of large NiO nanoparticles. A further increase in NiO size was observed when the reduction ramp rate was increased to 10 °C min^{-1} (Fig. S4). Thus, to obtain highly dispersed sub-nanometer Ni active sites, Ni loading and catalyst processing are critical, with the latter facilitating the slower formation and desorption of water in combination with stabilization of mobile Ni species [43].

XRD results in Fig. 2a show eight diffraction peaks at 28.5°, 33.2°, 47.6°, 56.5°, 59.2°, 69.4°, 76.7° and 79.1°, indicating a cubic fluorite structure of CeO_2 (JCPDS 34–0394), and indexed to (1 1 1), (2 0 0), (2 2 0), (3 1 1), (2 2 2), (4 0 0), (3 3 1) and (4 2 0) planes, respectively [44]. After introducing Ni on the surface of CeO_2 nanorods, the support crystal structure was unchanged, with no apparent Ni-containing crystal phases were detected due to the insensitivity of X-ray diffraction to small clusters [45]. This bulk analysis is in good agreement with the localised electron microscopy interpretation. The zoom area of XRD spectra

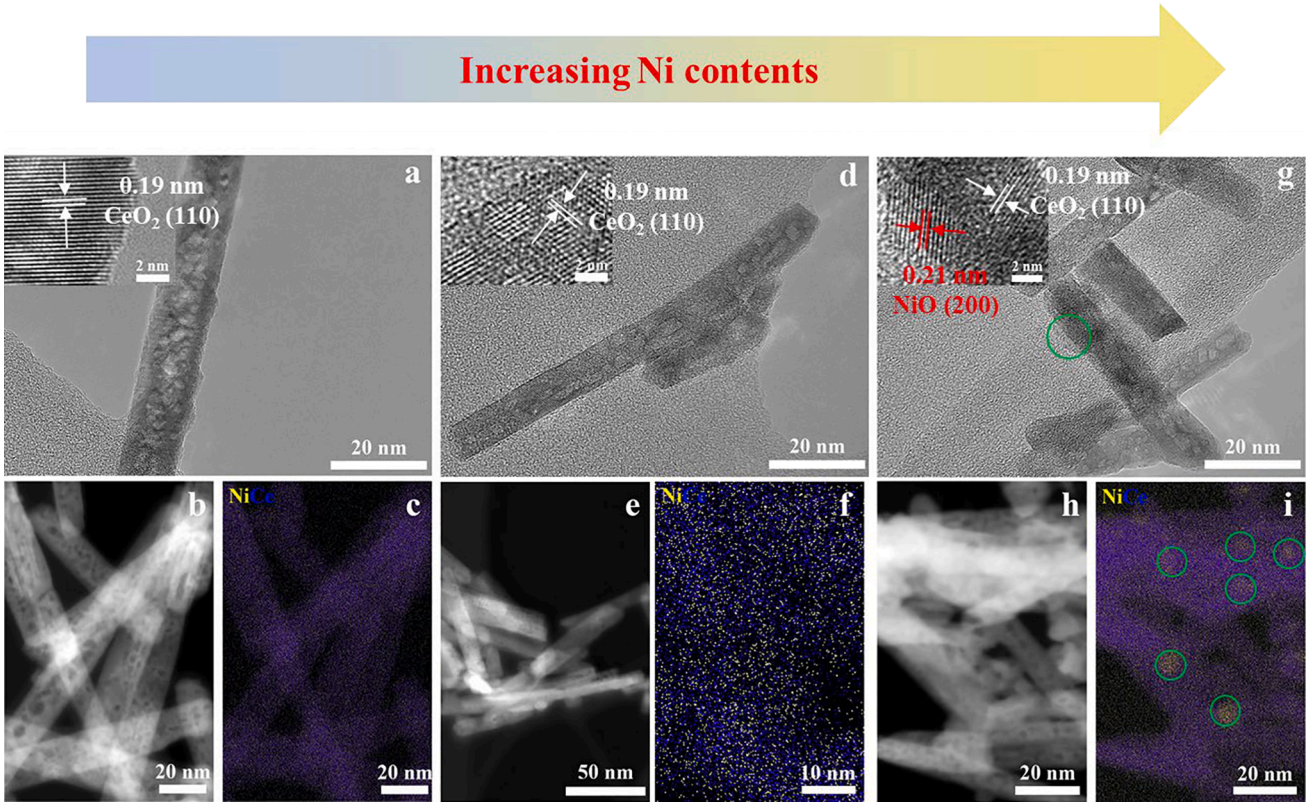

Fig. 1. HRTEM, HAADF-STEM images and EDX elemental mappings of (a-c) 0.5%Ni/CeO_2; (d-f) 1%Ni/CeO_2 and (g-i) 5%Ni/CeO_2.

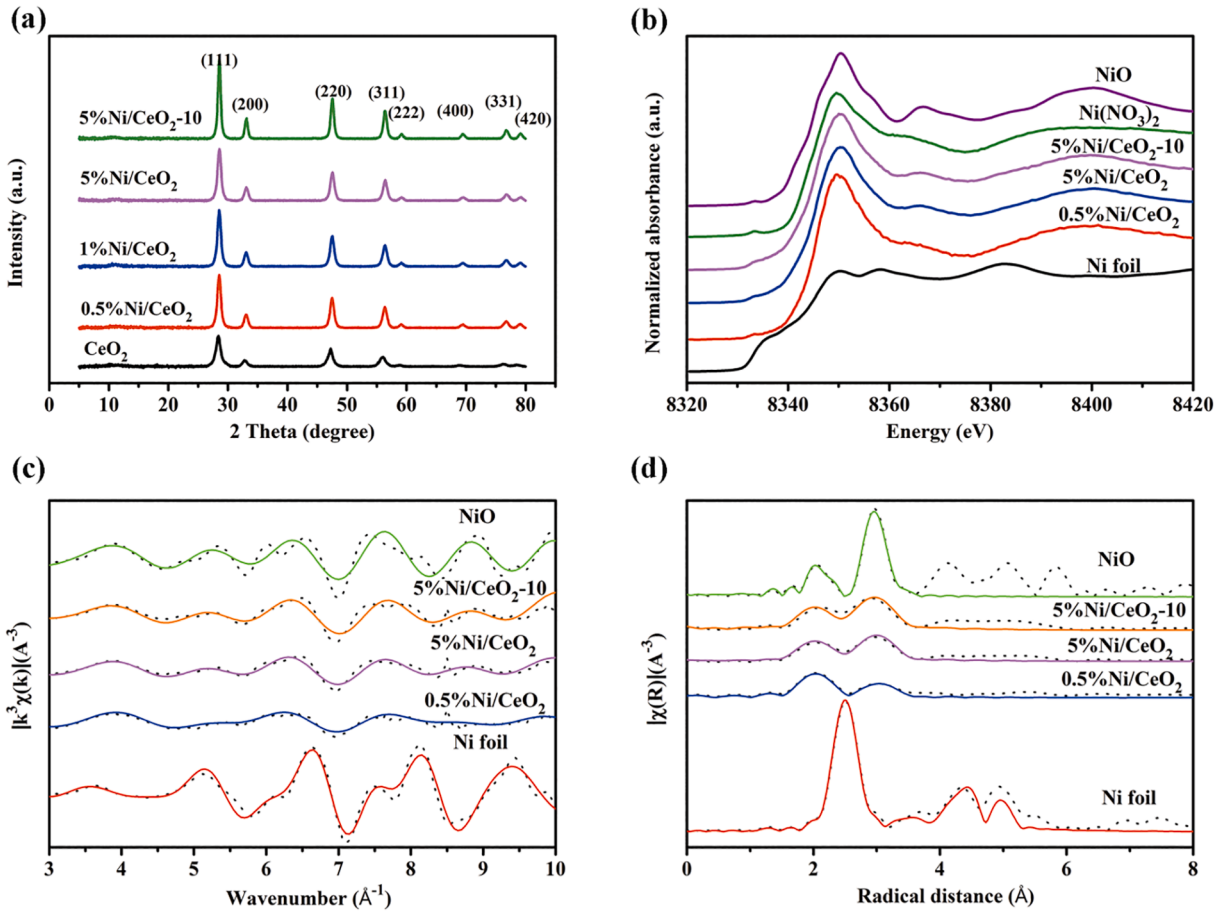

Fig. 2. (a) XRD patterns, (b) Normalized XANES spectra, (c) K-space EXAFS spectra, (d) K^3-weighted Fourier Transform EXAFS spectra.

ranging from 25 to 35° is shown in Fig. S5. It is found that the peak positions attributed to CeO_2 shifted to a higher angle after introducing of Ni species, which indicates a lattice contraction of Ni/CeO_2 catalysts. To further verify the local structures of the CeO_2 nanorod supported Ni clusters, Ni K-edge XAS was conducted. Edge position and X-ray absorption near-edge spectra (XANES) as shown in Fig. 2b reveal Ni to be present in the + 2 oxidation state as NiO for all loadings [46]. Fig. 2c and 2d show the K-space EXAFS spectra and corresponding Fourier Transform, and illustrate a good agreement between fit and raw data. The Fourier Transform of the EXAFS spectra confirm the oxidic nature of the Ni phase in all catalysts as identified by XANES, with major contributions from Ni-O and Ni-Ni (oxide 2nd shell) at 2.0 and 2.9 Å, respectively in Table 1. Furthermore, the absence of a significant scatter at 2.5 Å rules out the presence of Ni-Ni scatter from a metallic phase. EXAFS fitting confirms the lack of metallic Ni-Ni scatters in 0.5%Ni/CeO_2 and 5%Ni/CeO_2, with an increased contribution from a second shell NiO scatters in 5%Ni/CeO_2, reflecting an increase in NiO cluster size. Average NiO particle size from 1st shell CN are calculated to be 0.8 and 1.8 nm for 0.5%Ni/CeO_2 and 5%Ni/CeO_2, respectively [47], reflecting the same trend observed by electron microscopy. In contrast, fitting of 5%Ni/CeO_2-10 is significantly improved with the addition of a metallic Ni 1st shell scatter, indicating a degree of metallic Ni, albeit very minimal (coordination number of 1.9). We propose this indicates a metal-core oxide-shell structure, reflecting a further increase in Ni cluster size.

As reported in the literature, the peak centred at 466 cm^{-1} is assigned to the F_{2g} vibration mode of CeO_2 with fluorite structure [48]. The two weaker bands at 598 cm^{-1} and 1174 cm^{-1} corresponded to the defect-induced (D) vibrational mode from oxygen vacancies and the second-order longitudinal mode in CeO_2 lattice, respectively [49]. Therefore, Raman spectroscopy has been reported to probe surface electronic states and structural defects. Relative concentration of oxygen vacancies can be quantified from the intensity ratio of I_D/I_{F2g}. The

Table 1
EXAFS data fitting results.

Sample	Scatter coordination number				Interatomic distance Angstrom				Debye-Waller Factor				R Factor (%)
	1st Shell O (oxide)	1st Shell Ni (metal)	2nd Shell Ni (oxide)	2nd Shell Ni (metal)	1st Shell O (oxide)	1st Shell Ni (metal)	2nd Shell Ni (oxide)	2nd Shell Ni (metal)	1st Shell O (oxide)	1st Shell Ni (metal)	2nd Shell Ni (oxide)	2nd Shell Ni (metal)	
Ni foil	N/A	12.0	N/A	6.0	N/A	2.486	N/A	3.516	N/A	0.0064	N/A	0.0093	0.226
NiO	6.0	N/A	12.0	N/A	2.087	N/A	2.950	N/A	0.0057	N/A	0.0061	N/A	0.288
0.5%Ni/CeO_2	4.8	0.0	7.1	0.0	2.046	0.000	2.982	0.0	0.0056	0.0000	0.0164	0.0000	0.113
5%Ni/CeO_2	3.9	0.0	9.6	0.0	2.043	0.000	2.953	0.0	0.0050	0.0000	0.0129	0.0000	0.134
5%Ni/CeO_2-10	4.8	1.9	9.5	0.0	2.043	2.503	2.949	0.0	0.0078	0.0086	0.0126	0.0000	0.148

Raman spectra of prinstine CeO_2 and Ni/CeO_2 catalysts are shown in Fig. S6. It is found that the peak at 466 cm^{-1} exhibits a red shift in all the Ni/CeO_2 catalysts indicating a degree of Ni species incorporation within the ceria lattice [50]. However, the peaks at 598 cm^{-1} and 1174 cm^{-1} are not obvious as expected in our Raman spectra. Therefore further charaterizations should be conducted to confirm the variation of oxygen vacancies.

XPS analysis was used to investigate the CeO_2 supported catalysts' surface characteristics, as displayed in Fig. 3a-d. Ce 3d peaks were fit using a Shirley background and a cross-section of (1150.84 , −450 , 0 , 0) according to the model of Romeo *et al.* [37]. The Ce^{3+}/Ce^{4+} ratio was determined through integration of the peak model wherein Ce^{4+} is represented by 6 peaks (v, v'', v''', u, u'' and u''' centred at 882.2, 888.4, 897.8, 900.3, 907.7 and 916.4 eV, respectively) and Ce^{3+} is represented by 4 peaks (v^0, v', u^0, u' centred at 880.3, 884.3, 898.3 and 902.5 eV, respectively) [51]. The resultant ratios agree with that of the Raman spectra, in that the number of vacancies increases with increased Ni loading up to Ni 1%, before decreasing again with increased Ni loading, though remaining higher in number than that of the bare ceria as summarized in Table 2. The increase in vacancies upon the addition of Ni is due to a metal-oxide charge transfer from the nickel 4 s orbitals into the empty Ce 4f band, which reduces Ce^{4+} sites to Ce^{3+} sites [52]. The decrease in the number of vacancies at higher loadings may be attributed to the growth mode of Ni on CeO_2 and subsequent attenuation of the signal from Ce^{3+} regions relative to Ce^{4+} region by the small Ni clusters (which by the nature of Ni-CeO_2 interactions will tend to form over Ce^{3+} sites). Ni on CeO_2 has been known to form 2D-like structures at lower loadings before forming 3D clusters after a critical point, due to the strong interaction between Ni and CeO_2, causing significant wetting [53]. Once the formation of 3D particles begins, the increase in the number of new vacancy sites will cease to increase proportionally with Ni loading, and hence attenuation effects of Ce^{3+} 3d electrons will reduce the effective concentration.

Table 2
Metal dispersion and XPS data of the reduced catalysts.

Sample	Ni loading[a] wt.%	Ni dispersion[b] %	Ce 3d Ce^{3+}/Ce^{4+}	O 1s O_V/O_L
CeO_2	/	0	0.27	0.69
0.5%Ni/CeO_2	0.3	48	0.29	0.82
1%Ni/CeO_2	0.6	43	0.35	1.14
5%Ni/CeO_2	3.8	30	0.29	0.89
5%Ni/CeO_2-10	3.7	29	/	/

[a] Ni loading is determined by ICP.
[b] Ni dispersion obtained from CO chemisorption.

Analysis of the Ni 2p regions is complicated by the presence of some high energy structure from the Ce LMM auger which introduces difficulty in correctly modelling the background, particularly for the materials of a lower Ni loading. To compensate for this, a model Ce LMM background was developed by measuring the blank ceria across the energy range of the Ni 2p and used to correct the spectra in which Ni 2p and Ce LMM produced competing intensity (Fig. S7). Analysis of the raw, unaltered data appeared to suggest that the Ni was present solely as relatively large NiO clusters, exhibiting both the standard Ni^{2+} photoemission core line peak and the associated NiO_6 inter-cluster. However, when the contribution from the Ce LMM auger was removed via a

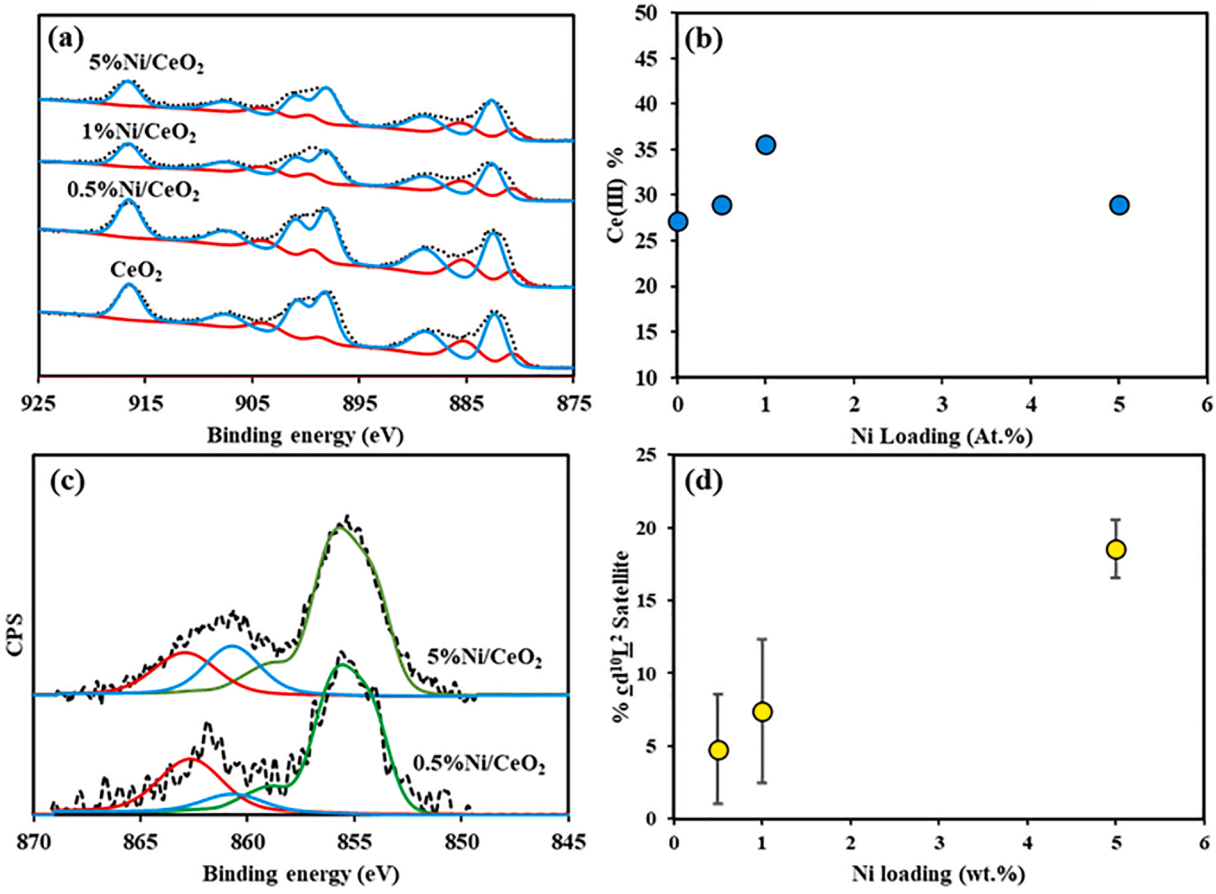

Fig. 3. (a) Ce 3d XPS spectra: blue profiles Ce^{4+} envelopes, red profiles Ce^{3+} envelopes, (b) Quantified Ce(III) % as a function of Ni loading, (c) Ni 2p XPS spectra and peak fitting curves following a SG-Quadratic auger subtraction process (Green-GS multiplet approximation of Ni^{2+} free ion [36], Blue-$\underline{c}d^{10}\underline{L}^2$ final-state satellite, Red-unscreened $\underline{c}d^8$ core-line) and (d) $\underline{c}d^{10}\underline{L}^2$ contribution as a function of Ni loading. (For interpretation of the references to colour in this figure legend, the reader is referred to the web version of this article.)

spectral subtraction method, the satellite intensity was altered and two states at + 7 eV and + 10 eV appeared. The + 7 eV satellite is commonly observed in clusters of multiple NiO_6 centres and can be attributed to the screening process of final state $\underline{c}d^{10}\underline{L}^2$ [54], while the highest energy peak may be attributed to the unscreened $\underline{c}d^8$ final state [55]. Four methods of background subtraction were performed as displayed in Fig. S8: (1) using the raw data from the Ni 2p region of the blank ceria (Fig. S9) following a Savitzky-Golay quadratic smoothing process and smoothing width of 17, (2) following a Gaussian smoothing process and smoothing width of 17, (3) developed using the resultant envelope from a component fit of the entire Ce LMM region, and (4) using a background trace from a Shirley-type background across the Ni 2p energy region (Fig. S10). We found good agreement between the different approaches, with only the S-type background trace reporting a higher proportion of the $\underline{c}d^{10}\underline{L}^2$ final-state, as shown in Fig. S11. Averages and standard deviations reported a general trend suggesting that as we move towards smaller clusters with decreasing Ni loading, the intensity from the $\underline{c}d^{10}\underline{L}^2$ final-state satellite decreases, which we attribute to the reduction in Ni coordination number as we approach sub-nanometer sizes, as indicated by the XAS measurements.

O 1 s regions as shown in Fig. S12 further confirm the presence of oxygen vacancies in the synthesized catalysts. The peaks at around 528.9 and 530.2 eV are assigned to the lattice oxygen (O_L) and oxygen deficient regions (O_V), respectively [48,56,57]. The ratio of O_V/O_L as shown in Table 2 is calculated to represent the abundance of oxygen vacancies in CeO_2-based catalysts. These values are 0.69, 0.82, 1.14 and 0.89 for pristine CeO_2, 0.5%Ni/CeO_2, 1%Ni/CeO_2, and 5Ni%/CeO_2, respectively. The results show that 1%Ni/CeO_2 has the most abundant

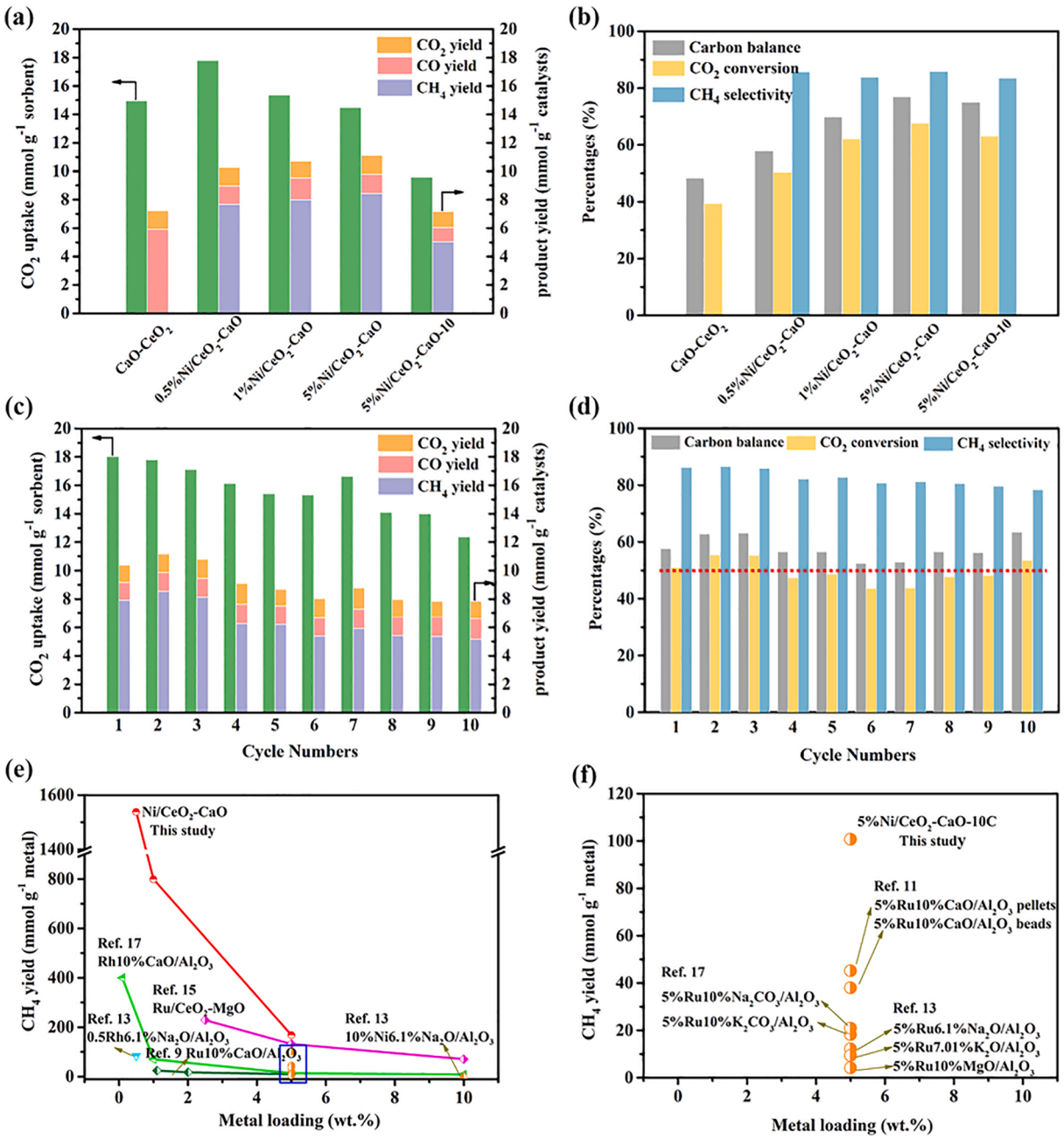

Fig. 4. (a, b) ICCU performance, (c, d) cyclic ICCU performance of 0.5%Ni/CeO_2-CaO, (e) the comparison of ICCU performance between this study and reported in the literature, (f) the enlarged view of blue area in Fig. 4e. (For interpretation of the references to colour in this figure legend, the reader is referred to the web version of this article.)

oxygen vacancy defects compared with the other catalysts, which is consistent with the analysis of Ce 3d.

3.2. ICCU performance of materials

The ICCU performance of the physical mixture of CaO and sub-nanometer Ni cluster supported on ceria nanorods were evaluated at 550 °C and 1 bar. The results are presented in Fig. 4 and Table 3. When the nickel-free CeO_2-CaO combination is used, a carbon capture capacity of 14.9 mmol g^{-1} is achieved, and CO is the sole product in the utilisation step. This partial reduction occurs over oxygen vacancies within the ceria, which absorb CO_2 and promote C-O bond cleavage through the oxidation of CeO_2 support as shown in Eq. (5) [8], with hydrogen reactivating the catalytic sites (Eq. (6)). The carbon balance and CO_2 conversion of CeO_2-CaO are only 48.5% and 39.5%, respectively (Fig. 4b). The obtained low carbon balance is accounted for the incomplete desorption of CO_2 from the adsorbent, shown by $CaCO_3$ content in Fig. S13. This observation agrees with the literature, which identified low activity but high selectivity for CO_2 reduction over ceria [58]. In addition, pristine CeO_2 can activate CO_2 to generate CO, but it is difficult to further hydrogenate the captured CO_2 to CH_4 (Fig. 4a and b), thus proving that CO_2 methanation is based on the synergistic effect of Ni and CeO_2 [48]. The addition of Ni to the system shows an increase in CO_2 conversion, which reaches 50.4%, 62.2% and 67.7% for 0.5%Ni/CeO_2-CaO, 1%Ni/CeO_2-CaO, and 5%Ni/CeO_2-CaO, respectively (Table 3).

$$CO_2 + Ce^{3+} \leftrightarrow CO + Ce^{4+} \quad (5)$$

$$H_2 + Ce^{4+} \leftrightarrow H_2O + Ce^{3+} \quad (6)$$

The addition of Ni sites, even at extreme low loadings of only 0.5 wt %, also drastically influences ICCU selectivity, shifting to CH_4 as the primary product as shown in Fig. 4b and Table 3. Furthermore, the yield of CH_4 in the ICCU process is significantly increased to 1540 mmol g^{-1} Ni over 0.5%Ni/CeO_2-CaO, which represents a significant enhancement compared to the materials as previously reported in the literature depicted in Fig. 4e. It is noted that the conversion of CO_2 using 5%Ni/CeO_2-CaO is only slightly higher than that using 0.5%Ni/CeO_2-CaO, although the difference of Ni loading is 10-fold. Therefore, 0.5%Ni/CeO_2-CaO exhibits a much higher CH_4 yield per gram of Ni active species (1540 mmol g^{-1} Ni) and TOF (188 h^{-1}) compared with other materials. The exceptional capacity of 0.5%Ni/CeO_2 for methane formation can be attributed to the high level of CO_2 reduction that occurs over oxygen vacancies on the ceria support, leaving Ni sites for CO hydrogenation to methane. When the heating rate of the reduction process is increased from 2 °C min^{-1} to 10 °C min^{-1}, the yield of CH_4 is decreased from 168 mmol g^{-1} Ni to 100 mmol g^{-1} Ni, which is probably due to the bigger Ni particle size of 5%Ni/CeO_2-10 resulting in fewer oxygen vacancies. This is further confirmed that the sub-nanometer catalysts exhibited higher activity in the ICCU process.

Table 3
ICCU performance of various materials.

Samples	CH_4 yield (mmol g^{-1} Ni)	CO_2 conversion(%)	CH_4 selectivity(%)	TOF[a](h^{-1})
CeO_2-CaO	0	39.5	0.00	/
0.5%Ni/CeO_2-CaO	1540	50.4	85.8	188
1%Ni/CeO_2-CaO	800	62.2	83.8	109
5%Ni/CeO_2-CaO	168	67.7	85.9	33
5%Ni/CeO_2-CaO-10	100	63.1	83.6	20

[a] TOF = number of moles CH_4 product /(number of Ni active centres*reaction time)

The cyclic stability, in particular at elevated temperatures, is crucial for the industrial application of sub-nanometer catalysts in the ICCU process. Fig. 4c and d, as well as Fig. S14 show the stability of 0.5%Ni/CeO_2-CaO and 1%Ni/CeO_2-CaO after 10 cycles of ICCU process at 550 °C, respectively. The initial CH_4 yield of 0.5%Ni/CeO_2-CaO after the 1st cycle of ICCU process is 7.9 mmol $gcat.^{-1}$ and the CO_2 conversion and CH_4 selectivity are 51.0% and 86.2%, respectively. After 10 cycles of the ICCU process, even though the CH_4 yield is decreased to 5.2 mmol $gcat.^{-1}$, the CO_2 conversion and CH_4 selectivity are still as high as 53.5% and 78.4%, respectively, which indicate that the sub-nanometer catalysts exhibited a good stability. Through the comparison of ICCU performance after 10 cycles, the CO_2 conversion using 0.5%Ni/CeO_2-CaO is 53.5% which is higher than 1%Ni/CeO_2-CaO (50.4%). This is attributed to the high Ce^{3+}/Ce^{4+} ratio of 0.5%Ni/CeO_2-CaO (0.30), while 1%Ni/CeO_2-CaO has a Ce^{3+}/Ce^{4+} ratio of 0.24, as shown in Fig. S15, further implying that the oxygen vacancies are important for the conversion of captured CO_2 during the ICCU process. In addition, XPS of spent materials reveal a nickel state which is hydroxidic in nature (Fig. S16), as evidenced by subtle shifts to a higher binding energy, accompanied by a significant decrease in the satellite structure at ~+3 and ~+7 eV compared with the oxidic fresh material [59]. Moreover, both the spent 0.5%Ni/CeO_2-CaO and 1%Ni/CeO_2-CaO displayed an obvious peak centered at 700 °C as shown in Fig. S17, which is attributed to decomposition of $CaCO_3$, further indicating the incomplete desorption of CO_2 from the adsorbent. However, we do not find any peaks assigned to the coke deposition because the coke always be burned below 600 °C. Therefore, the deactivation of the physical mixing materials during the ICCU process might be attributed to the sintering of sorbents because the capacity of carbon capture is decreased from 18.0 mmol g^{-1} to 12.4 mmol g^{-1} after 10 cycles of the ICCU process.

3.3. Mechanism study

The in-situ DRIFTS study was used to investigate the interaction between highly dispersed Ni clusters and oxygen vacancies over Ni/CeO_2 sub-nanometer catalysts. After introducing CO_2 (1st stage of ICCU), the IR bands centered at 2326, 2360, 3597, 3631, 3698 and 3734 cm^{-1} come out immediately as shown in Fig. 5a, indicating the adsorption of gas-phase CO_2 [60,61]. In addition, the IR features developed at 877, 1070, 1450 and 1540 cm^{-1} represent different vibrational modes of bicarbonates [14], and the peak centered at 1780 cm^{-1} is the C = O vibration mode of calcite carbonate [62]. The peaks centered at 2500, 2850 and 2950 cm^{-1} are assigned to the formate species, which was derived from the hydrogenation of bicarbonate assisted by the hydrogen on Ni particles in reduced catalysts as previously reported [63]. These results indicate the formation of formate, calcite carbonate and bicarbonate species after CO_2 capture stage during the ICCU process caused by the chemical reaction between CaO sites and the introduced CO_2 gas phase. The IR bands centred at 2114 and 2176 cm^{-1} are attributed to the CO species due to the oxygen vacancies in CeO_2 will direct cleavage CO_2. After switching the feed gas to H_2, the intensities of the above-mentioned calcite carbonate and formate species remain almost unchanged. However, the peak intensity of CO species are gradually decreased, while the IR band at 3016 cm^{-1} attributed to CH_4 species can be detected as shown in Fig. 5b, implying that CO is probably intermediate and conveted to CH_4 during the 2nd stage of ICCU. This is because the formed CO species react with dissociated hydrogen on Ni metallic particles to release CH_4 in the presence of hydrogen [64]. An in-situ DRIFTS experiment included CO adsorption and subsequent H_2 conversion is conducted to verify the reaction schemes and the results are diaplayed in Fig. 5c. It is found that after introducing CO into the cell, IR bands at 2114 and 2176 cm^{-1} come out immediately. After swithcing the feed gas to H_2, a peak centered at 3016 cm^{-1} assigned to the CH_4 species can be detected. This further confirms that CO is converted to CH_4 over the 1%Ni/CeO_2-CaO.

DFT calculations further investigated the role of nickel on the

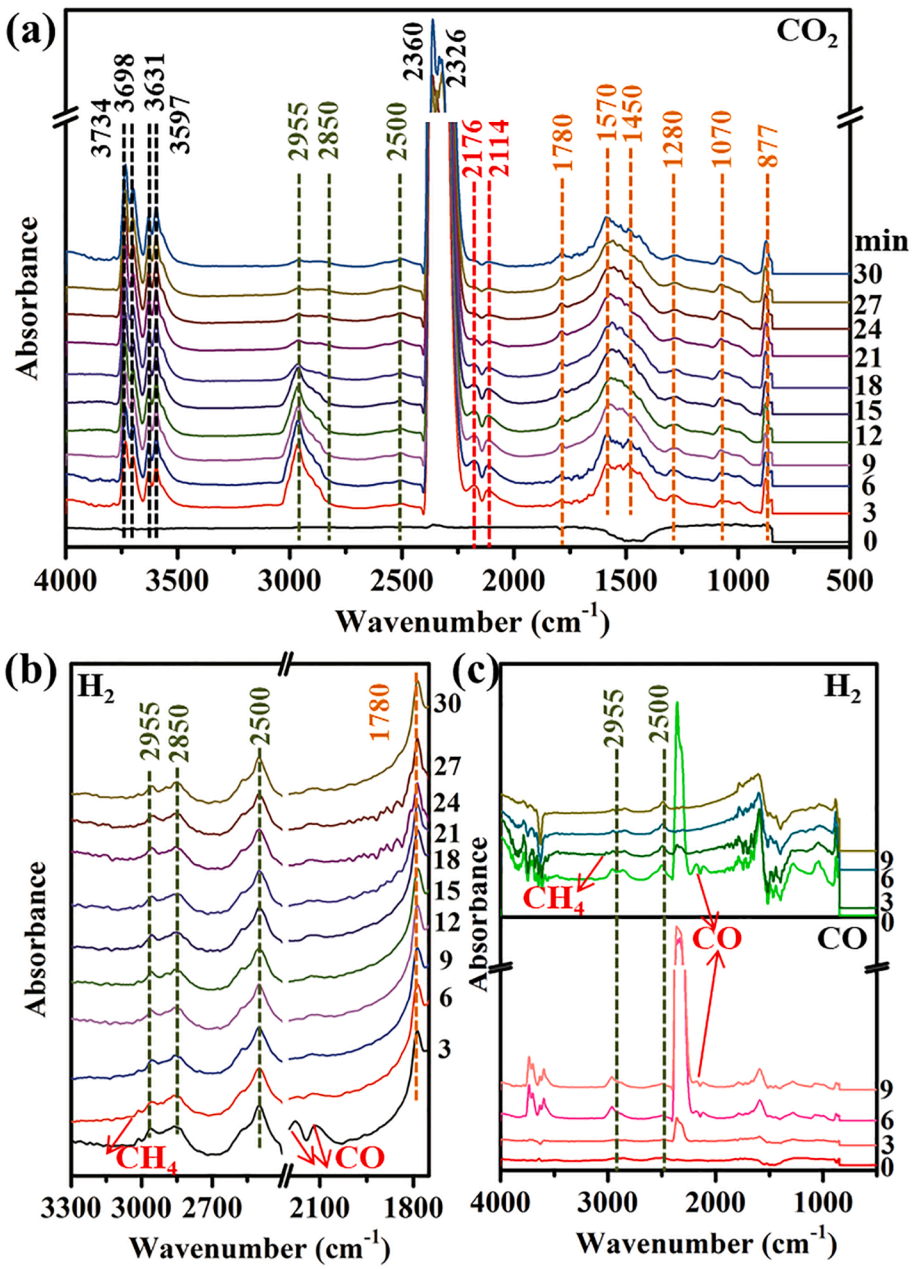

Fig. 5. In-situ DRIFTS spectra of the species formed over 1%Ni/CeO_2-CaO: (a, b) CO_2 capture stage and H_2 conversion stage during the ICCU process, respectively, (c) CO adsorption and subsequent H_2 conversion.

selectivity of the overall process. Based on the HRTEM (Fig. 1), (1 1 0) lattice plane is the preferentially exposed surface of CeO_2 nanorods. Therefore, a ceria (1 1 0) supercell structure with a single oxygen vacancy (Ov-CeO_2(1 1 0)) was constructed and optimised, on top of which a sub-nanometer Ni active site was supported, as shown in Fig. 6. After optimisation, CO adsorption energies were calculated for both systems, revealing E_b of −0.23 eV and −1.88 eV on Ov-CeO_2(1 1 0) and Ni/CeO_2(1 1 0), respectively. The low CO binding strength to Ov-CeO_2(1 1 0) reflects a high potential for spontaneous desorption, as observed by *in-situ* IR spectra that no obvious peaks assigned to the CO adsorption on CeO_2 are observed (Fig. S18). This accounts for the selectivity of CO_2 reduction over ceria nanorods (Fig. 4). With the deposition of Ni cluster, the binding strength of CO on Ni/CeO_2(1 1 0) surface is significantly enhanced, which increases the likelihood of further reaction and accounts for the shift to methane for Ni doped ceria nanorods.

From our experimental results and DFT calculation, the mechanism of CO_2 methanation over Ni/CeO_2 catalysts can be summarized as follow (Fig. 7): Firstly, CO_2 molecules are chemisorbed on the partially reduced NiO-CeO_2 interface, where most of the C = O bonds are broken together with the oxygen transferring to the ceria support to restore the oxygen balance. These oxygens move around in the ceria lattice through the abundant vacancies and provide available sites for further CO_2 chemisorption. Afterwards, different reaction pathways will be created. A fraction of carbon species are converted to CO through the reverse water gas shift reaction and then hydrogenated to CH_4; simultaneously, part of the oxygens removed upon the double bonds breaking are replaced by catalyst oxygen and released as CO or CO_2, leaving reduced sites on the catalyst again. Therefore, the main products of Ni/CeO_2 sub-nanometer catalysts are CO and CH_4.

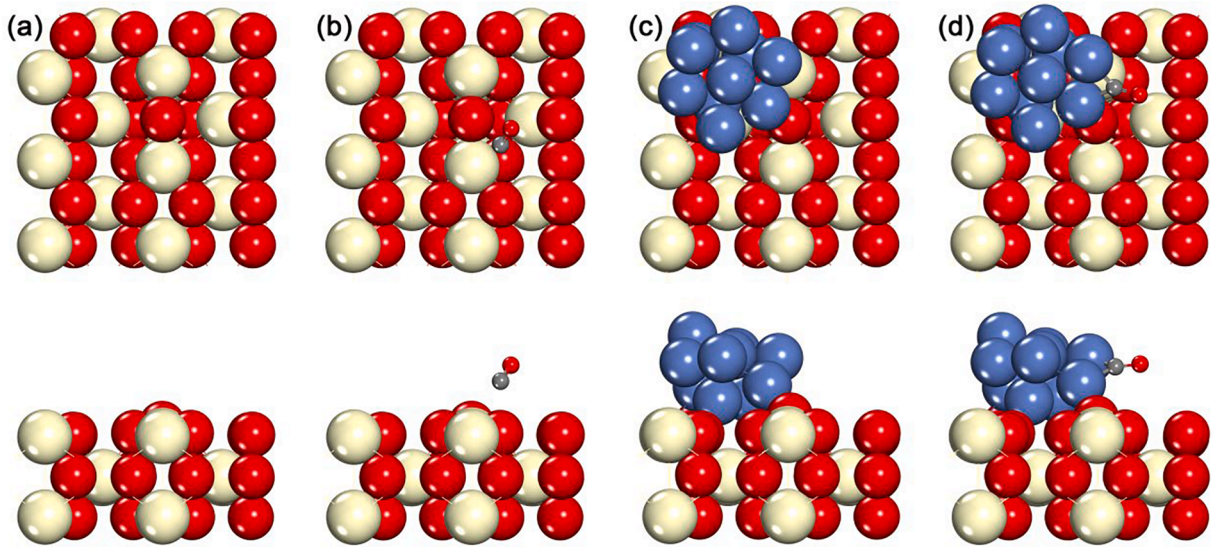

Fig. 6. Top and side view of the optimized structures of (a) CeO_2(1 1 0) with a O vacancy (Ov-CeO_2(1 1 0)), (b) Ov-CeO_2(1 1 0) with the adsorption of CO, (c) CeO_2(1 1 0) supported Ni cluster (Ni/CeO_2(1 1 0)) and (d) Ni/CeO_2(1 1 0) with the adsorption of CO. The yellow, red, grey and blue balls represent the Ce, O, C and Ni atoms. (For interpretation of the references to colour in this figure legend, the reader is referred to the web version of this article.)

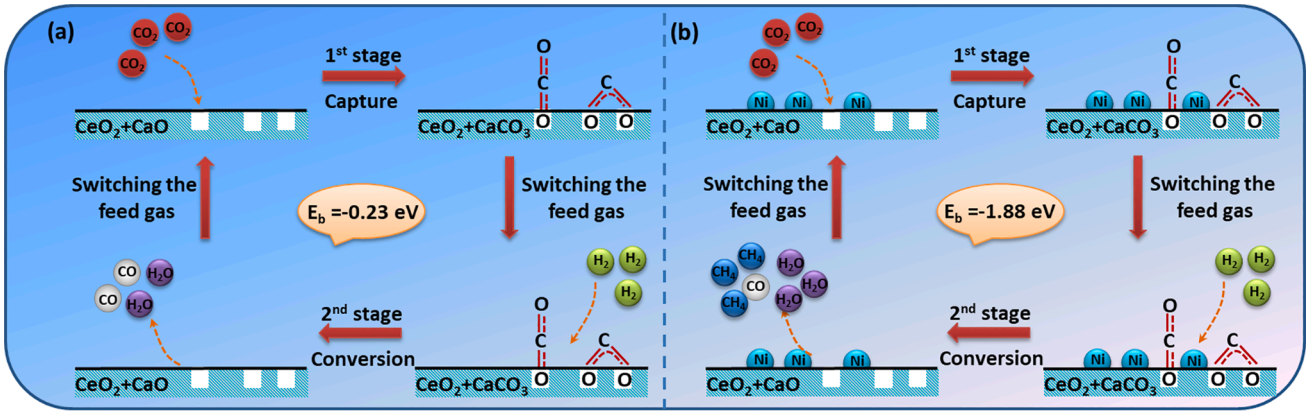

Fig. 7. Reaction mechanism during the ICCU process: (a) CeO_2-CaO, (b) Ni/CeO_2-CaO.

4. Conclusions

We have shown the synergistic coupling of earth-abundant materials for ICCU. A physical mixture of CaO and Ni/CeO_2, as adsorbent and catalysts, respectively, shows excellent performance for capturing CO_2 from flue gas, via adsorption by CaO to form $CaCO_3$, and subsequent release under a hydrogen-rich gas stream. Upon CO_2 desorption, which regenerates the adsorbent for subsequent cycles, catalytic CO_2 reduction is facilitated over Ni doped ceria nanorods. The yield and selectivity values of CH_4 over our optimum system 0.5%Ni/CeO_2-CaO of 1540 mmol g^{-1} Ni and 85.8%, respectively, coupled with high stability over 10 ICCU cycles, can be ascribed to the cooperative catalytic performance of highly dispersed Ni clusters and oxygen vacancies present on Ni doped ceria nanorods. CO_2 is reduced to CO over oxygen vacancies on CeO_2, CO desorbs and diffuses to Ni sites where hydrogenation to CH_4, the major product, occurs. These results are expected to have a broad implication on the design and development of efficient and cost-effective materials for ICCU.

CRediT authorship contribution statement

Hongman Sun: Conceptualization, Investigation, Visualization, Formal analysis, Writing – original draft. **Yu Zhang:** Conceptualization, Formal analysis, Writing – review & editing. **Chunfen Wang:** Conceptualization, Formal analysis, Writing – review & editing. **Mark A. Isaacs:** Investigation, Writing – review & editing. **Ahmed I. Osman:** Investigation, Writing – review & editing. **Yehong Wang:** Investigation, Writing – review & editing. **David Rooney:** Investigation, Writing – review & editing. **Youhe Wang:** Conceptualization, Formal analysis, Writing – review & editing. **Zifeng Yan:** Conceptualization, Formal analysis, Writing – review & editing. **Christopher M.A. Parlett:** Investigation, Visualization, Writing – review & editing. **Feng Wang:** Supervision, Conceptualization, Writing – review & editing. **Chunfei Wu:** Supervision, Conceptualization, Writing – review & editing.

Declaration of Competing Interest

The authors declare that they have no known competing financial interests or personal relationships that could have appeared to influence the work reported in this paper.

Acknowledgements

This work was financially supported by the European Union's Horizon 2020 research and innovation programme under the Marie Skłodowska-Curie Grant Agreement (No. 823745), the Fundamental

Research Funds for the Central Universities (No. 21CX06013A) and National Natural Science Foundation of China (No. 22102215). The authors wish to acknowledge the Diamond Light Source for provision of beamtime (UK Catalysis Hub SP19850), National Natural Science Foundation of China (No. 22025206, 21961130378), the Newton Advanced Fellowships (NAF\R1\191267), the Ministry of Science and Technology of the People's Republic of China (No. 2018YFE0117300) and Key Projects of China National Key R&D Plan (No. 2018YFE0118200).

Appendix A. Supplementary data

Supplementary data to this article can be found online at https://doi.org/10.1016/j.cej.2022.135394.

References

[1] H. Sun, C. Wu, B. Shen, X. Zhang, Y. Zhang, J. Huang, Progress in the development and application of CaO-based adsorbents for CO_2 capture-a review, Mater. Today Sustain. 1 (2018) 1–27.
[2] L. Liu, S. Das, T. Chen, N. Dewangan, J. Ashok, S. Xi, A. Borgna, Z. Li, S. Kawi, Low temperature catalytic reverse water-gas shift reaction over perovskite catalysts in DBD plasma, Appl. Catal. B: Environ. 265 (2020), 118573.
[3] W. Gao, S. Liang, R. Wang, Q. Jiang, Y. Zhang, Q. Zheng, B. Xie, C.Y. Toe, X. Zhu, J. Wang, Industrial carbon dioxide capture and utilization: state of the art and future challenges, Chem. Soc. Rev. 49 (2020) 8584–8686.
[4] C. Yang, S. Liu, Y. Wang, J. Song, G. Wang, S. Wang, Z.J. Zhao, R. Mu, J. Gong, The Interplay between Structure and Product Selectivity of CO_2 Hydrogenation, Angew Chem (2019).
[5] L.R. Winter, E. Gomez, B. Yan, S. Yao, J.G. Chen, Tuning Ni-catalyzed CO_2 hydrogenation selectivity via Ni-ceria support interactions and Ni-Fe bimetallic formation, Appl. Catal. B: Environ. 224 (2018) 442–450.
[6] F.N. Ridha, D.Y. Lu, R.T. Symonds, S. Champagne, Attrition of CaO-based pellets in a 0.1 MWth dual fluidized bed pilot plant for post-combustion CO_2 capture, Powder Technol. 291 (2016) 60–65.
[7] D. Li, Y. Zhou, Y. Shen, W. Sun, Q. Fu, H. Yan, D. Zhang, Experiment and simulation for separating CO_2/N_2 by dual-reflux pressure swing adsorption process, Chem. Eng. J. 297 (2016) 315–324.
[8] H. Sun, J. Wang, J. Zhao, B. Shen, J. Shi, J. Huang, C. Wu, Dual functional catalytic materials of Ni over Ce-modified CaO sorbents for integrated CO_2 capture and conversion, Appl. Catal. B: Environ. 244 (2019) 63–75.
[9] M.S. Duyar, M.A.A. Trevino, R.J. Farrauto, Dual function materials for CO_2 capture and conversion using renewable H_2, Appl. Catal. B: Environ. 168 (2015) 370–376.
[10] M.A. Arellano-Treviño, N. Kanani, C.W. Jeong-Potter, R.J. Farrauto, Bimetallic catalysts for CO_2 capture and hydrogenation at simulated flue gas conditions, Chem. Eng. J. 375 (2019), 121953.
[11] Q. Zheng, R. Farrauto, A. Chau Nguyen, Adsorption and methanation of flue gas CO_2 with dual functional catalytic materials: a parametric study, Ind. Eng. Chem. Res. 55 (24) (2016) 6768–6776.
[12] A. Bermejo-López, B. Pereda-Ayo, J.A. González-Marcos, J.R. González-Velasco, Mechanism of the CO_2 storage and in situ hydrogenation to CH_4. Temperature and adsorbent loading effects over Ru-CaO/Al_2O_3 and Ru-Na_2CO_3/Al_2O_3 catalysts, Appl. Catal. B: Environ. 256 (2019), 117845.
[13] M.A. Arellano-Treviño, Z. He, M.C. Libby, R.J. Farrauto, Catalysts and adsorbents for CO_2 capture and conversion with dual function materials: Limitations of Ni-containing DFMs for flue gas applications, J. CO_2 Util. 31 (2019) 143–151.
[14] L. Proaño, E. Tello, M.A. Arellano-Trevino, S. Wang, R.J. Farrauto, M. Cobo, In-situ DRIFTS study of two-step CO_2 capture and catalytic methanation over Ru, "N_a2O"/A_l2_O3 Dual Functional Material, Appl. Surf. Sci. 479 (2019) 25–30.
[15] H. Sun, Y.u. Zhang, S. Guan, J. Huang, C. Wu, Direct and highly selective conversion of captured CO_2 into methane through integrated carbon capture and utilization over dual functional materials, J. CO_2 Util. 38 (2020) 262–272.
[16] S. Sun, Z. Lv, Y. Qiao, C. Qin, S. Xu, C. Wu, Integrated CO_2 capture and utilization with CaO-alone for high purity syngas production, Carbon Capture Science & Technology 1 (2021), 100001.
[17] N. Gao, K. Chen, C. Quan, Development of CaO-based adsorbents loaded on charcoal for CO_2 capture at high temperature, Fuel 260 (2020), 116411.
[18] B. González, J. Blamey, M.J. Al-Jeboori, N.H. Florin, P.T. Clough, P.S. Fennell, Additive effects of steam addition and HBr doping for CaO-based sorbents for CO_2 capture, Chem. Eng. Process. 103 (2016) 21–26.
[19] Y. Xu, C. Shen, B. Lu, C. Luo, F. Wu, X. Li, L. Zhang, Study on the effect of NaBr modification on CaO-based sorbent for CO_2 capture and SO_2 capture, Carbon Capture Science & Technology 1 (2021), 100015.
[20] M.S. Duyar, S. Wang, M.A. Arellano-Treviño, R.J. Farrauto, CO_2 utilization with a novel dual function material (DFM) for capture and catalytic conversion to synthetic natural gas: An update, J. CO_2 Util. 15 (2016) 65–71.
[21] T. Chen, Z. Wang, L. Liu, S. Pati, M.H. Wai, S. Kawi, Coupling CO_2 separation with catalytic reverse water-gas shift reaction via ceramic-carbonate dual-phase membrane reactor, Chem. Eng. J. 379 (2020), 122182.
[22] C.-S. Chen, C.S. Budi, H.-C. Wu, D. Saikia, H.-M. Kao, Size-tunable Ni nanoparticles supported on surface-modified, cage-type mesoporous silica as highly active catalysts for CO_2 hydrogenation, ACS Catal. 7 (12) (2017) 8367–8381.
[23] A. Solis-Garcia, J.F. Louvier-Hernandez, A. Almendarez-Camarillo, J.C. Fierro-Gonzalez, Participation of surface bicarbonate, formate and methoxy species in the carbon dioxide methanation catalyzed by ZrO_2-supported Ni, Appl. Catal. B: Environ. 218 (2017) 611–620.
[24] Y. Wang, Y.-Q. Su, E.J.M. Hensen, D.G. Vlachos, Finite-Temperature Structures of Supported Subnanometer Catalysts Inferred via Statistical Learning and Genetic Algorithm-Based Optimization, ACS Nano 14 (10) (2020) 13995–14007.
[25] E. Guan, J. Ciston, S.R. Bare, R.C. Runnebaum, A. Katz, A. Kulkarni, C. X. Kronawitter, B.C. Gates, Supported metal pair-site catalysts, ACS Catal. 10 (16) (2020) 9065–9085.
[26] J. Resasco, L. DeRita, S. Dai, J.P. Chada, M. Xu, X. Yan, J. Finzel, S. Hanukovich, A. S. Hoffman, G.W. Graham, Uniformity Is Key in Defining Structure-Function Relationships for Atomically Dispersed Metal Catalysts: The Case of Pt/CeO_2, J. Am. Chem. Soc. 142 (1) (2019) 169–184.
[27] Y. Ma, B. Chi, W. Liu, L. Cao, Y. Lin, X. Zhang, X. Ye, S. Wei, J. Lu, Tailoring of the proximity of platinum single atoms on CeO_2 using phosphorus boosts the hydrogenation activity, ACS Catal. 9 (9) (2019) 8404–8412.
[28] A. Wang, J. Li, T. Zhang, Heterogeneous single-atom catalysis, Nat. Rev. Chem. 2 (6) (2018) 65–81.
[29] F. Wang, S. He, H. Chen, B. Wang, L. Zheng, M. Wei, D.G. Evans, X. Duan, Active site dependent reaction mechanism over Ru/CeO_2 catalyst toward CO_2 methanation, J. Am. Chem. Soc. 138 (19) (2016) 6298–6305.
[30] K. Chang, H. Zhang, M.-J. Cheng, Q.i. Lu, Application of Ceria in CO_2 Conversion Catalysis, ACS Catal. 10 (1) (2020) 613–631.
[31] J.A.H. Dreyer, P. Li, L. Zhang, G.K. Beh, R. Zhang, P.H.L. Sit, W.Y. Teoh, Influence of the oxide support reducibility on the CO_2 methanation over Ru-based catalysts, Appl. Catal. B: Environ. 219 (2017) 715–726.
[32] Y.u. Tang, Y. Wei, Z. Wang, S. Zhang, Y. Li, L. Nguyen, Y. Li, Y. Zhou, W. Shen, F. F. Tao, P. Hu, Synergy of single-atom Ni_1 and Ru_1 sites on CeO_2 for dry reforming of CH_4, J. Am. Chem. Soc. 141 (18) (2019) 7283–7293.
[33] H.-X. Mai, L.-D. Sun, Y.-W. Zhang, R. Si, W. Feng, H.-P. Zhang, H.-C. Liu, C.-H. Yan, Shape-selective synthesis and oxygen storage behavior of ceria nanopolyhedra, nanorods, and nanocubes, J. Phys. Chem. B 109 (51) (2005) 24380–24385.
[34] E.T. Santos, C. Alfonsín, A.J.S. Chambel, A. Fernandes, A.P. Soares Dias, C.I. C. Pinheiro, M.F. Ribeiro, Investigation of a stable synthetic sol-gel CaO sorbent for CO_2 capture, Fuel 94 (2012) 624–628.
[35] H. Sun, J. Wang, X. Liu, B. Shen, C.A. Parlett, G.O. Adwek, E. John Anthony, P. T. Williams, C. Wu, Fundamental studies of carbon capture using CaO-based materials, J. Mater. Chem. A 7 (16) (2019) 9977–9987.
[36] R. Gupta, S. Sen, Calculation of multiplet structure of core p-vacancy levels. II, Phys. Rev. B 12 (1) (1975) 15.
[37] M. Romeo, K. Bak, J. El Fallah, F. Le Normand, L. Hilaire, XPS study of the reduction of cerium dioxide, Surf. Interface Anal. 20 (6) (1993) 508–512.
[38] G. Kresse, J. Furthmuller, Efficient iterative schemes for ab initio total-energy calculations using a plane-wave basis set, Physical review B 54 (16) (1996) 11169–11186.
[39] J.P. Perdew, K. Burke, M. Ernzerhof, Generalized gradient approximation made simple, Physical review letters 77 (18) (1996) 3865–3868.
[40] G. Kresse, D. Joubert, From ultrasoft pseudopotentials to the projector augmented-wave method, Physical review b 59 (3) (1999) 1758–1775.
[41] F.N. Ridha, V. Manovic, A. Macchi, M.A. Anthony, E.J. Anthony, Assessment of limestone treatment with organic acids for CO_2 capture in Ca-looping cycles, Fuel Process. Technol. 116 (2013) 284–291.
[42] X. Ma, Y. Li, C. Chi, W. Zhang, J. Shi, L. Duan, CO_2 Capture Performance of Mesoporous Synthetic Sorbent Fabricated Using Carbide Slag under Realistic Calcium Looping Conditions, Energy Fuels 31 (7) (2017) 7299–7308.
[43] D. Koningsberger, J.d. Graaf, A. Van Dillen, K. De Jong, Preparation of highly dispersed Pt particles in zeolite Y with a narrow particle size distribution: Characterization by hydrogen chemisorption, TEM, EXAFS spectroscopy, and particle modeling, J. Catal. 203(2) (2001) 307-321.
[44] J. An, Y. Wang, J. Lu, J. Zhang, Z. Zhang, S. Xu, X. Liu, T. Zhang, M. Gocyla, M. Heggen, Acid-promoter-free ethylene methoxycarbonylation over Ru-clusters/ceria: the catalysis of interfacial Lewis acid-base pair, J. Am. Chem. Soc. 140 (11) (2018) 4172–4181.
[45] F. Wang, C. Li, X. Zhang, M. Wei, D.G. Evans, X. Duan, Catalytic behavior of supported Ru nanoparticles on the 1 0 0},{1 1 0}, and {1 1 1 facet of CeO2, J. Catal. 329 (2015) 177–186.
[46] C.M.A. Parlett, A. Aydin, L.J. Durndell, L. Frattini, M.A. Isaacs, A.F. Lee, X. Liu, L. Olivi, R. Trofimovaite, K. Wilson, C. Wu, Tailored mesoporous silica supports for Ni catalysed hydrogen production from ethanol steam reforming, Catal. Commun. 91 (2017) 76–79.
[47] A. Kuzmin, J. Chaboy, EXAFS and XANES analysis of oxides at the nanoscale, IUCrJ 1 (6) (2014) 571–589.
[48] R.-P. Ye, Q. Li, W. Gong, T. Wang, J.J. Razink, L. Lin, Y.-Y. Qin, Z. Zhou, H. Adidharma, J. Tang, A.G. Russell, M. Fan, Y.-G. Yao, High-performance of nanostructured Ni/CeO_2 catalyst on CO_2 methanation, Appl. Catal. B: Environ. 268 (2020) 118474, https://doi.org/10.1016/j.apcatb.2019.118474.
[49] X. Du, D. Zhang, L. Shi, R. Gao, J. Zhang, Morphology dependence of catalytic properties of Ni/CeO_2 nanostructures for carbon dioxide reforming of methane, J. Phys. Chem. C 116 (18) (2012) 10009–10016.
[50] N. Wang, W. Qian, W. Chu, F. Wei, Crystal-plane effect of nanoscale CeO_2 on the catalytic performance of Ni/CeO_2 catalysts for methane dry reforming, Catal. Sci. Technol. 6 (10) (2016) 3594–3605.

[51] Z. Li, M. Li, J. Ashok, S. Kawi, NiCo@NiCo phyllosilicate@CeO_2 hollow core shell catalysts for steam reforming of toluene as biomass tar model compound, Energ. Convers, Manage. 180 (2019) 822–830.
[52] J. Carrasco, L. Barrio, P. Liu, J.A. Rodriguez, M.V. Ganduglia-Pirovano, Theoretical studies of the adsorption of CO and C on Ni (111) and Ni/CeO_2 (111): evidence of a strong metal-support interaction, J. Phys. Chem. C 117 (16) (2013) 8241–8250.
[53] Y. Zhou, J. Zhou, Interactions of Ni nanoparticles with reducible CeO_2 (111) thin films, J. Phys. Chem. C 116 (17) (2012) 9544–9549.
[54] M.A. van Veenendaal, G.A. Sawatzky, Nonlocal screening effects in 2p x-ray photoemission spectroscopy core-level line shapes of transition metal compounds, Phys. Rev. Lett. 70 (16) (1993) 2459–2462.
[55] D. Alders, F.C. Voogt, T. Hibma, G.A. Sawatzky, Nonlocal screening effects in 2p x-ray photoemission spectroscopy of NiO (100), Phys. Rev. B 54 (11) (1996) 7716–7719.
[56] N.C.D. Nath, J.-J. Lee, Intercalation-type electrodes of copper-cobalt oxides for high-energy-density supercapacitors, Journal of Electroanalytical Chemistry 861 (2020), 113947.
[57] N.C.D. Nath, H.W. Jeong, D.S. Han, H. Park, J.-J. Lee, Facile Electrochemical Synthesis of Highly Efficient Copper-Cobalt Oxide Nanostructures for Oxygen Evolution Reactions, Journal of The Electrochemical Society 167 (2) (2020) 026510, https://doi.org/10.1149/1945-7111/ab6a80.
[58] B. Dai, S. Cao, H. Xie, G. Zhou, S. Chen, Reduction of CO_2 to CO via reverse water-gas shift reaction over CeO_2 catalyst, Korean J. Chem. Eng. 35 (2) (2018) 421–427.
[59] M.C. Biesinger, L.W. Lau, A.R. Gerson, R.S.C. Smart, The role of the Auger parameter in XPS studies of nickel metal, halides and oxides, Phys. Chem. Chem. Phys. 14 (7) (2012) 2434–2442.
[60] A.M. Abdel-Mageed, S. Eckle, H. Anfang, R.J. Behm, Selective CO methanation in CO_2-rich H2 atmospheres over a Ru/zeolite catalyst: The influence of catalyst calcination, J. Catal. 298 (2013) 148–160.
[61] G. Garbarino, D. Bellotti, E. Finocchio, L. Magistri, G. Busca, Methanation of carbon dioxide on Ru/Al_2O_3: catalytic activity and infrared study, Catal. Today 277 (2016) 21–28.
[62] J.T. Kloprogge, R.L. Frost, L. Hickey, Infrared emission spectroscopic study of the dehydroxylation of some hectorites, Thermochim. Acta 345 (2) (2000) 145–156.
[63] F. Zhu, L. Zhu-Ge, G. Yang, S. Zhou, Iron-Catalyzed Hydrogenation of Bicarbonates and Carbon Dioxide to Formates, ChemSusChem 8 (4) (2015) 609–612.
[64] Y. Yu, Y.M. Chan, Z. Bian, F. Song, J. Wang, Q. Zhong, S. Kawi, Enhanced performance and selectivity of CO_2 methanation over g-C_3N_4 assisted synthesis of Ni CeO_2 catalyst: Kinetics and DRIFTS studies, Int. J. Hydrogen Energy 43 (32) (2018) 15191–15204.